

NukesFormers: Unpaired Hyperspectral Image Generation with Non-Uniform Domain Alignment

Jiaojiao Li

jjli@xidian.edu.cn

Shiyao Duan

syduan_1@stu.xidian.edu.cn

Haitao XU

xuhaitao@nssc.ac.cn

Rui Song

rsong@xidian.edu.cn

Abstract

The inherent difficulty in acquiring accurately co-registered RGB-hyperspectral image (HSI) pairs has significantly impeded the practical deployment of current data-driven Hyperspectral Image Generation (HIG) networks in engineering applications. Gleichzeitig, the ill-posed nature of the aligning constraints, compounded with the complexities of mining cross-domain features, also hinders the advancement of unpaired HIG (UnHIG) tasks. In this paper, we conquer these challenges by modeling the UnHIG to range space interaction and compensations of null space through Range-Null Space Decomposition (RND) methodology. Specifically, the introduced contrastive learning effectively aligns the geometric and spectral distributions of unpaired data by building the interaction of range space, considering the consistent feature in degradation process. Following this, we map the frequency representations of dual-domain input and thoroughly mining the null space, like degraded and high-frequency components, through the proposed Non-uniform Kolmogorov-Arnold Networks. Extensive comparative experiments demonstrate that it establishes a new benchmark in UnHIG.

1. Introduction

Hyperspectral imaging finds extensive applications in numerous fields, including drug analysis [25], remote sensing detection [31] and image fusion [11]. Nevertheless, due to the inherent limitations of imaging equipment, acquiring an adequate number of hyperspectral images (HSIs) with high quality, compared with RGBs or multispectral images (MSIs), is excessively time-consuming and prohibitively expensive. Furthermore, hardware enhancements tend to occur at a sluggish pace, thereby highlighting the pressing need to rely on software or algorithms to obtain a substantial number of HSIs. Currently, as one of the most efficient technologies for acquiring HSIs, Hyperspectral Image Genera-

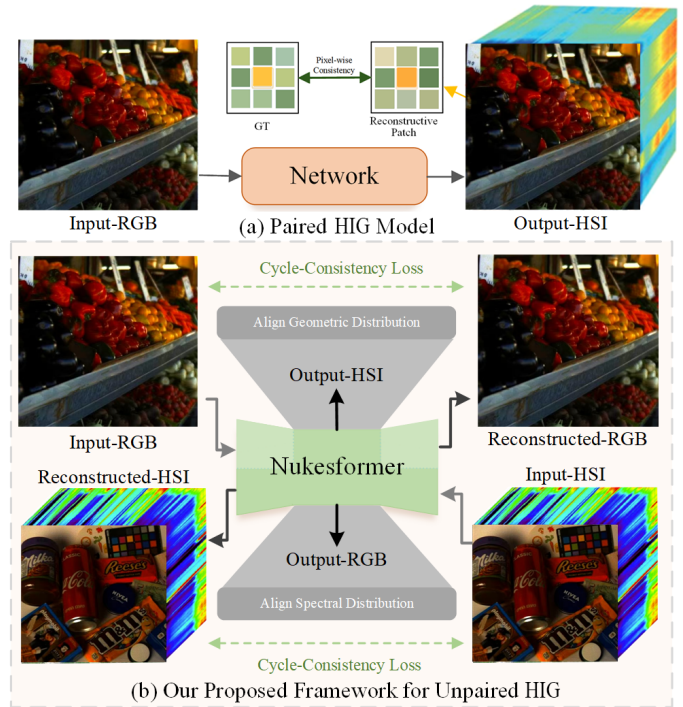


Figure 1. (a) The conventional framework of paired HIG, which utilizes ground truth (GT) to build direct pixel-wise consistency. (b) Our proposed NukesFormer for unpaired HIG without GT, which establishes indirect constraint with cycle-consistency and dual-dimensional contrastive prior module (DCPM).

tion (HIG) enables the generation with both fine spatial and spectral resolution from a single RGB or MSI[5, 16, 35, 40], which is modeled to learn inverse mapping from HSI.

Similar to other tasks, the data-driven learning strategy in HIG methods has recently witnessed a significant improvement in reconstruction performance [4, 12], as depicted in Fig.1(a). Nonetheless, the reliability of fully-supervised HIG is often reliant on the amount and diversity of paired

and registered RGB-HSI or MSI-HSI training sets, which are challenging to obtain in practical work yet.

To tackle these challenges, numerous studies have proposed training HIG models exploiting unsupervised [14, 43], semi-supervised [15], and unpaired methods [28, 34], thereby mitigating the dependency on high-quality paired data with well co-registration. Among these approaches, unpaired HIG (UnHIG) has garnered increasing attention due to the prevalence of non-registered HSIs in practical applications [29, 34]. However, UnHIG is constrained by the absence of natural cross-domain interactions, leading to a serious non-uniform status between the corresponding information in dual domains. Additionally, the lack of human-annotated hints renders the valuable hyperspectral priors largely inaccessible during the training phase. As a result, critical degraded features, predominantly comprising high-frequency components, are either discarded or overwhelmed in existing approaches. Unfortunately, the challenges still seriously block the performance of UnHIG at present.

Drawing inspiration from the advances of Range-Null Space Decomposition (RND) methodologies in various tasks [9, 38], we explore the feasibility of leveraging RND to address the challenges of UnHIG. Specifically, we aim to decompose the inverse high-dimensional mapping into range-space interactions encompassing consistent features, and null-space compensations targeting degraded and high-frequency components. Within this framework, range-space interactions function as an indirect spectral and geometric constraint by encapsulating consistent or inconsistent information inherent to intra-domain and intra-scene relationships. On the other hand, the null-space compensation focuses on mining weak and attenuated high-frequency components of null space, thereby enhancing the overall reconstruction process.

In this paper, we propose a novel and lightweight framework for UnHIG by integrating cross-domain interactions and leveraging spectral characteristic information. Concretely, the unpaired data is systematically decomposed into continuous components termed the range space, and attenuated components referred to as the null space, via RND methodology. Subsequently, the framework employs a cycle-based architecture to capture intra-domain attributes, while utilizing dual-dimensional contrastive learning to aggregate continuous elements within the range space effectively. Moreover, building on Kolmogorov-Arnold Networks (KANs) [3, 24], a dedicated Non-Uniform Matrix Object-Aware Mechanism dynamically shifts the B-Spline function to enhance null-space compensation, facilitating high-dimensional fitting with robust guidance. Finally, extensive experimental evaluations demonstrate that the proposed method achieves state-of-the-art performance across various benchmarks.

The key contributions of this work are summarized as follows:

- We introduce a novel contrastive priori framework for UnHIG, which decomposes the generation process into null-space mining and range-space alignment, enabling superior high-frequency compensation and effective cross-domain interaction.
- To adaptively extract high-frequency components obscured within the null space, we propose a Non-Uniform KANs (NukesFormers), which generates flexible and adaptive rational bases that precisely capture vulnerable yet crucial characteristic bands.
- A dual-branch contrastive structure is further proposed that independently calibrates both geometric and spectral distributions to facilitate effective cross-domain interaction in range space, leveraging HSI and RGB or MSI from different scenes to build reliable constraint.

2. Related Work

2.1. Hyperspectral Image Generation

From the data-orientated perspective, HIG is categorized into three distinct categories: supervised [5, 16, 19], prior-based unsupervised [20, 43], and unpaired methods.

Representing the most stringent data requirements and the most direct method of constraint construction, the supervised HIG utilizes many paired RGB-HSIs to construct the point-to-point constraint. Zhao et al. proposed that HRNet employs the residual dense block to obtain a larger receptive field and deploys the PixelShuffle to achieve feature fusion between layers [40]. Consequently, a self-supervised HIG framework was proposed [43], which uses SRF and pre-trained semantic segmentation networks to construct point-level constraints, resulting in impressive results.

The aforementioned approaches neglect the vast collection of existing HSIs that have been captured and stored, due to the absence of essential prior, which implies that unpaired methods potentially reactivate the overlooked data to satisfy the requirements of industrial deployment.

2.2. Unpaired Methods in Computer Vision

The paradox between a vast amount of redundant unpaired data and the challenge of constructing appropriate constraints has consistently impeded the progress of computer vision, leading to the wastage of collected data [7, 23]. Initially, a Bayesian framework was constructed to establish the connection of two domains [30], utilizing Markov random fields in image-to-image translation.

Additionally, the cycle-based [42] approaches employ paired generators and discriminators to simulate domain information extraction, and introduce cycle consistency to achieve intuitive constraints [13]. In deraining, contrastive prior is utilized to construct positive and negative sample

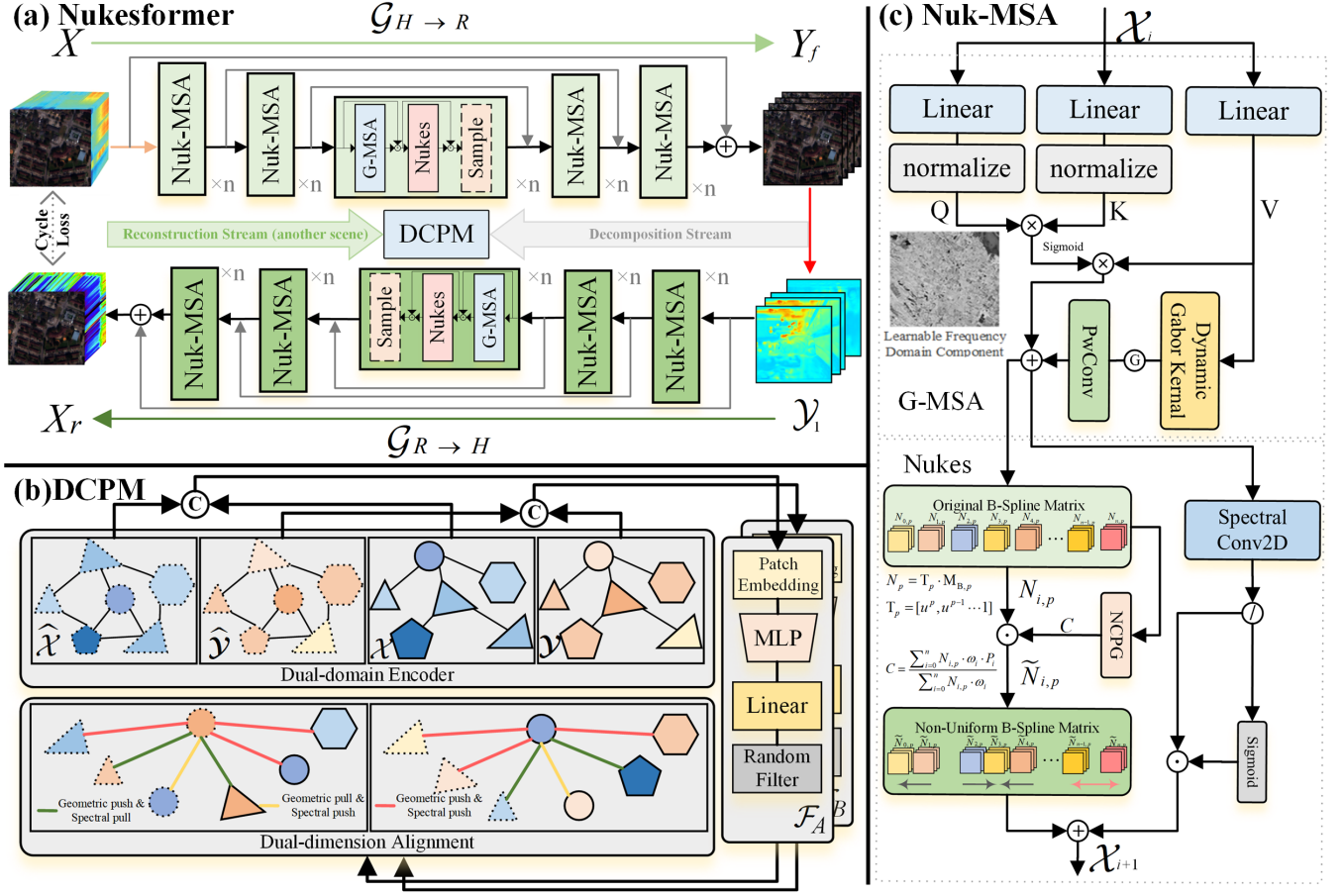


Figure 2. The overall framework of proposed NukesFormer of decomposition stream, where the reconstruction stream in (a) derives from another NukesFormer, leveraging shared parameters. (b) DCPM utilizes the dual-dimensional contrastive prior to pull ($\rightarrow\leftarrow$) similar geometric and spectral distributions and push ($\leftarrow\rightarrow$) different components. (c) The non-uniform B-Spline matrix and G-MSA are dedicated to capturing multi-frequency information from spectral dimension.

pairs to extract and remove rain signals [7]. By utilizing contrastive learning methods to address patch information at the same position in images and retrieve information from distant parts, effective constraints are indirectly achieved [27].

In a similar vein, HIG tasks also strive to leverage ample unmatched HSI and RGB data [43]. This underscores the critical need to develop a model capable of achieving stable training and robust cross-scene interaction while relying solely on unpaired data.

3. Method

In this section, we first present the MetaFormer [37] architecture equipped with Non-uniform KANs (NukesFormers) tailored for the UnHIG. In NukesFormers, the "Degradation" phase (Fig.2a) deploys the dynamic Gabor transformer to mine high-frequency components and the cas-

coding Non-uniform KANs embedded Multi-head Self-attention (Nuk-MSA) to compensate for the attenuated null space in the RGB domain. Then, we introduce the dual-dimensional contrastive prior module (DCPM), designed to build the reliable constraint with range space.

3.1. NukesFormers for UnHIG

Unlike paired HIG, we employ an acquired HSI denoted $\mathbf{X} \in \mathbb{R}^{C \times H \times W}$ along with an RGB of a different scene, represented as $\hat{\mathbf{Y}} \in \mathbb{R}^{3 \times H \times W}$, in UnHIG. Obviously, UnHIG cannot directly leverage GT to extract latent feature representations of HSI domain, but a large amount of unpaired RGB-HSIs still bury a unified degradation-reconstruction process as below:

$$\mathbf{Y} = \mathbf{D}\mathbf{X} + \mathbf{N}_c \quad \hat{\mathbf{Y}} = \mathbf{D}\hat{\mathbf{X}} + \mathbf{N}_e \quad (1)$$

where $\mathbf{D} \in \mathbb{R}^{3 \times C}$ and $\mathbf{N}_e \in \mathbb{R}^{3 \times H \times W}$ are depicted as the SRF and camera noise. Furthermore, \mathbf{Y} means the RGB in

the same scene as \mathbf{X} .

Omitting \mathbf{N}_c considerations, the dual direction mapping process can be portrayed using the inverse operation (pseudo-inverse) of \mathbf{D} as $\mathbf{D}^\dagger \in \mathbb{R}^{C \times 3}$, as illustrated in the RND methodology [33].

$$\begin{aligned}\mathbf{X} &\equiv \mathbf{D}^\dagger \mathbf{D} \mathbf{X} + (\mathbf{I} - \mathbf{D}^\dagger \mathbf{D}) \mathbf{X} \\ \hat{\mathbf{Y}} &\equiv \mathbf{D} \mathbf{D}^\dagger \hat{\mathbf{Y}} + (\mathbf{I} - \mathbf{D} \mathbf{D}^\dagger) \hat{\mathbf{Y}}\end{aligned}\quad (2)$$

which decomposes the HSIs into range space $\mathbf{D}^\dagger \mathbf{D} \mathbf{X}$ and null space $(\mathbf{I} - \mathbf{D}^\dagger \mathbf{D}) \mathbf{X}$. Evidently, the cycle-based framework can be built by degradation-reconstruction operators $\mathbf{D}^\dagger \mathbf{D}(\cdot)$ as long as $\mathbf{I} - \mathbf{D}^\dagger \mathbf{D} = \mathbf{0}$, which implies that \mathbf{D} must be orthogonal (this, however, is infeasible since $C > 3$). As a consequence, we redefine the equation as $\min \|\mathbf{X} - \mathbf{D}^\dagger \mathbf{D} \mathbf{X}\|_2^2$, s.t., $\|(\mathbf{I} - \mathbf{D}^\dagger \mathbf{D}) \mathbf{X}\|_2^2 = \epsilon_0$, ϵ_0 represents a value infinitesimally close to zero. Obviously, the above constraints can be simplified to $\min \|\mathbf{D}^\dagger \mathbf{D} \mathbf{X} - \mathbf{X}\|_2^2$. Then the "Reconstruction" phase possesses a similar consequent, which establishes the cycle-based constraint as follows.

$$\begin{aligned}\mathcal{L}_{cyc}(\mathbf{X}, \hat{\mathbf{Y}}) &= \mathbb{E}_{r \sim R} [\|\mathcal{G}_{R \rightarrow H \rightarrow R}(\mathbf{X}) - \mathbf{X}\|_2^2] \\ &+ \mathbb{E}_{h \sim H} [\|\mathcal{G}_{H \rightarrow R \rightarrow H}(\hat{\mathbf{Y}}) - \hat{\mathbf{Y}}\|_2^2]\end{aligned}\quad (3)$$

in which $\mathcal{G}_{R \rightarrow H \rightarrow R}$ and $\mathcal{G}_{H \rightarrow R \rightarrow H}$ represent the joint models of reconstruction-degradation ($\mathcal{G}_{R \rightarrow H} - \mathcal{G}_{H \rightarrow R}$) and degradation-reconstruction operations with NukesFormers, as depicted in Fig.2a.

3.2. Non-uniform KANs Embedded Multi-head Self-attention

To obtain the consistent feature of the RGB-HSI domain buried in unpaired data, we introduce the NukesFormer, accurately capturing geometric distributions and essential high-frequency information in null space. As depicted in Fig.2a, spectral degradation $\mathcal{G}_{H \rightarrow R}$ and reconstruction $\mathcal{G}_{R \rightarrow H}$ are individually modelled using paired NukesFormers, which are then integrated into dual domains through a shared parameter mechanism.

$$\begin{aligned}\mathbf{Y}_f &= \mathcal{G}_{H \rightarrow R}(\mathbf{X} | \theta_{H \rightarrow R}) \quad \mathbf{X}_r = \mathcal{G}_{R \rightarrow H}(\mathbf{Y}_f | \theta_{R \rightarrow H}) \\ \hat{\mathbf{X}}_f &= \mathcal{G}_{R \rightarrow H}(\hat{\mathbf{Y}} | \theta_{R \rightarrow H}) \quad \hat{\mathbf{Y}}_r = \mathcal{G}_{H \rightarrow R}(\hat{\mathbf{X}}_f | \theta_{H \rightarrow R})\end{aligned}\quad (4)$$

in which $\theta_{R \rightarrow H}$ and $\theta_{H \rightarrow R}$ represent the learnable parameter. In the "Degradation" phase, acquired HSIs \mathbf{X} undergo a modelled degradation process to produce the corresponding fake-RGB \mathbf{Y}_f . Subsequently, a NukesFormer simulates the reconstruction process, converting the fake RGB back to a recovery-HSI \mathbf{X}_r . In the "Reconstruction" phase, the RGB of another scene experiences a similar process.

Nuk-MSA. However, one can anticipate that $\mathcal{G}_{H \rightarrow R}$ might yield high-frequency components of HSI domain that are

overly degraded, due to the abstraction of intermediate feature as the network deepens. Initially, we sample the RGB or HSI to obtain the original feature.

$$\mathcal{X}_1 = \text{Conv}_{1 \times 1}(\mathbf{X}) \quad \mathcal{Y}_1 = \text{Conv}_{1 \times 1}(\mathbf{Y}_f) \quad (5)$$

Subsequently, these features undergo a progressive refinement process via a series of cascaded Nuk-MSA.

$$\begin{aligned}\mathcal{X}_{i+1} &= \mathbf{M}_{DGK}(\mathcal{X}_j | \theta_{en,i+1}^{H \rightarrow R}) \quad \mathcal{Y}_{i+1} = \mathbf{M}_{DGK}(\mathcal{Y}_i | \theta_{en,i+1}^{R \rightarrow H}) \\ \mathcal{X}_{j+1} &= \mathbf{M}_{DGK}(\text{Map}(\text{Concat}(\mathcal{X}_j, \mathcal{X}_i)) | \theta_{de,j+1}^{H \rightarrow R}) \\ \mathcal{Y}_{j+1} &= \mathbf{M}_{DGK}(\text{Map}(\text{Concat}(\mathcal{Y}_j, \mathcal{Y}_i)) | \theta_{de,j+1}^{R \rightarrow H})\end{aligned}\quad (6)$$

$\mathcal{X}_i, \mathcal{Y}_i$ are the intermediate feature of every encoder in NukesFormer, and $\mathcal{X}_j, \mathcal{Y}_j$ represent the feature of the corresponding level in decoder.

$$\mathbf{Y}_f = \mathcal{X}_F + \mathcal{X}_1 \quad \mathbf{X}_r = \mathcal{Y}_F + \mathcal{Y}_1 \quad (7)$$

Finally, a skip connect is utilized to gain the \mathbf{Y}_f and \mathbf{X}_r .

Gabor Kernel based Multi-head Self-attention (G-MSA). In contrast to frequency domain transformations that rely on FFT or similar techniques [10, 17, 21, 22], the utilization of Gabor kernels enables the model to focus more on local and needed frequency intervals, which effectively mitigates the issue of high-frequency information being overshadowed.

Specifically, we employ the spectral multi-head self-attention (MSA) to generate the requisite query $\mathbf{Q} \in \mathbb{R}^{HW \times C}$, key $\mathbf{K}^T \in \mathbb{R}^{C \times HW}$, and value \mathbf{V} through linear operations, thus obtaining global spectral features.

$$\begin{aligned}\mathbf{Q}, \mathbf{K}, \mathbf{V} &= \text{Linear}(\mathcal{X}_i | \theta_Q, \theta_K, \theta_V) \\ \mathbf{A} &= \text{Softmax}(\mathbf{K}^T \mathbf{Q}) \quad \mathcal{X}_{i,msa} = \mathbf{V} \mathbf{A}\end{aligned}\quad (8)$$

in which θ_Q, θ_K and θ_V represent the learnable parameters.

To mine deeper into high-frequency feature in varying scenes, a scene-adaptive Gabor kernel is embedded by dynamic convolution layer [8, 18, 26] to facilitate feature generation from various directions and frequency domain intervals. Notably, the range of intervals is contingent upon the specific objects under consideration.

$$g_m(x, y | f_m) = \exp\left(-\frac{x_\theta^2 + (y_\theta/f_m)^2}{2\sigma^2}\right) \quad (9)$$

where f_m is the m -th dynamic frequency parameter to control the interval of the Gabor kernel, $x_\theta = x \cos(\theta) + y \sin(\theta)$ and $y_\theta = -x \sin(\theta) + y \cos(\theta)$. And x and y mean the horizontal and vertical position coordinates in spatial dimension.

As depicted in Fig.2c, the Gabor kernels are embedded into a dynamic depthwise convolution to lightweight. Subsequently, the multiple windows captured are mapping to one

learnable frequency domain component for every channel.

$$\begin{aligned} \mathbf{V}_{f,m} &= \mathbf{V} * g_m(x, y) \quad \mathbf{V}_f = \{\mathbf{V}_{f,1}, \mathbf{V}_{f,2}, \dots\} \\ \mathcal{X}_{i,frv} &= \text{Conv}(\text{GELU}(\mathbf{V}_f)) \end{aligned} \quad (10)$$

by which the frequency value $\mathbf{V}_f \in \mathbb{R}^{H \times W \times CM}$ are mapping to $\mathcal{X}_{i,frv} \in \mathbb{R}^{H \times W \times C}$. After that, the final feature in G-MSA is obtained with the element-wise addition operation.

$$\mathcal{X}_{i,f} = \mathcal{X}_{i,frv} + \mathcal{X}_{i,msa} \quad (11)$$

Non-uniform KANs Networks (Nukes) In the conventional MetaFormer architecture, multi-head self-attention (MSA) generates multiple attention maps that are typically integrated via concatenated MLP or CNN-based feed-forward networks (FFN). However, they often neglect the intricate nature of spectral features and the capacity to capture high-dimensional characteristics critical for hyperspectral tasks. Therefore, UnHIG imposes heightened requirements on capacity of building high-dimensional mapping in FFN.

In response to the challenges of high-dimensional spectral fitting in UnHIG, we introduce a lightweight and interpretable framework, Nukes. Leveraging advanced KANs, that streamline the traditionally redundant linear weights and nonlinear activation functions into a compact set of initial learnable parameters ω . These parameters are used within a recursive approach to generate multi-level B-spline basis functions $\mathbf{N}_{i,p}$.

$$\mathbf{N}_{i,0}(x) = \begin{cases} 1, & x_i \leq x < x_{i+1} \\ 0, & \text{otherwise} \end{cases} \quad (12)$$

$$\begin{aligned} \mathbf{N}_{i,p}(x) &= \frac{x - x_i}{x_{i+p} - x_i} \mathbf{N}_{i,p-1}(x) \\ &+ \frac{x_{i+p+1} - x}{x_{i+p+1} - x_{i+1}} \mathbf{N}_{i+1,p-1}(x) \end{aligned} \quad (13)$$

While KANs offer a powerful recursive framework, they are inherently GPU-unfriendly due to recursive dependencies. To enhance parallel computation and efficiency, we reformulate the recursive process into matrix form as Eq. 14, achieving significantly improved computational performance on GPU architectures.

$$\begin{aligned} \mathbf{N}_p &= \mathbf{T}_p \mathbf{M}_{B,p} \\ \mathbf{T}_p &= [\mathbf{u}^p, \mathbf{u}^{p-1}, \dots, 1] \end{aligned} \quad (14)$$

where \mathbf{N}_p , \mathbf{T}_p and $\mathbf{M}_{B,p}$ represent the weight matrix of control points, multi-stage index matrix and B-spline basis matrix constructed by learnable parameters.

However, capturing essential high-dimensional spectral features in UnHIG remains challenging due to limited non-linear representation and uniform reference point placement along the coordinate axis. To address this, we propose a

Non-Uniform Control Point Generator (NCPG), which dynamically adjusts control points' relative attraction and exclusion forces within the Nukes curve. During training, control points \mathbf{P}_i are adaptively concentrated on the most salient regions of the high-dimensional spectral features.

$$\mathbf{Nuk}(x) = \frac{\sum_{i=0}^n \mathbf{N}_{i,p}(x) \cdot \omega_i \cdot \mathbf{P}_i}{\sum_{i=0}^n \mathbf{N}_{i,p}(x) \cdot \omega_i} \quad (15)$$

in which $\mathbf{Nuk}(x)$ is the non-uniform B-spline curve.

Finally, the another branch with spectral CNN extract the low-frequency information to complement the geometric features as Eq. 16.

$$\begin{aligned} [\mathcal{X}_{i,up}, \mathcal{X}_{i,dw}] &= \text{Chunk}(\text{Spec-Conv}(\mathcal{X}_{i,f})) \\ \mathcal{X}_{i+1} &= \alpha \mathbf{Nuk}(\mathcal{X}_{i,f}) + \mathcal{X}_{i,up} \cdot \text{sigmoid}(\mathcal{X}_{i,dw}) \end{aligned} \quad (16)$$

where α is the learnable ratio.

In summary, Nukes aims to minimize parameter usage while maintaining interpretability, allowing it to adaptively fit and learn critical high-dimensional features and mapping relationships in hyperspectral tasks.

3.3. Dual-Dimensional Contrastive Prior Module

In pursuit of stable constraint, the DCPM is employed to facilitate interaction between the two domains, by building the relationship between RGB and HSI of distinct scenes with range space. However, distinguishing from existing methods [6, 7], DCPM introduces dual-dimensional contrastive priors, which are dedicated to resolving with concurrently handling mutual information from both domains, which are embedded with significantly different feature distribution.

Consequently, DCPM incorporates two auxiliary encoders ($\mathcal{F}_A(\cdot)$ and $\mathcal{F}_B(\cdot)$) that map the output of final stage's Nuk-MSA to the spectral and geometric features of latent spaces, in which the auxiliary encoders are constituted by multilayer perceptron (MLP) with the activation function. Illustrating with the "Degradation" phase, the features extracted from both domains are divided into patches. Then, a single patch from one domain is designated as the query code \mathbf{f} . Subsequent patches from both domains are then partitioned into positive \mathbf{f}^+ and negative codes \mathbf{f}^- . It's noteworthy that patches from both domains are utilized in distinguishing positive from negative samples, marking a deviation from previous methods [27]. After filters are applied to randomly extract relevant patches, the resultant samples undergo spectral contrastive learning.

$$\begin{aligned} \mathcal{L}_{spec}(\mathcal{G}_{R \rightarrow H}, \mathcal{G}_{H \rightarrow R}) &= \\ \mathbb{E}_{h \sim H, r \sim R} &\left[-\log \frac{\text{sam}(\mathbf{f}, \mathbf{f}^+)}{\text{sam}(\mathbf{f}, \mathbf{f}^+) + \sum_{i=1}^N \text{sam}(\mathbf{f}, \mathbf{f}_i^-)} \right] \end{aligned} \quad (17)$$

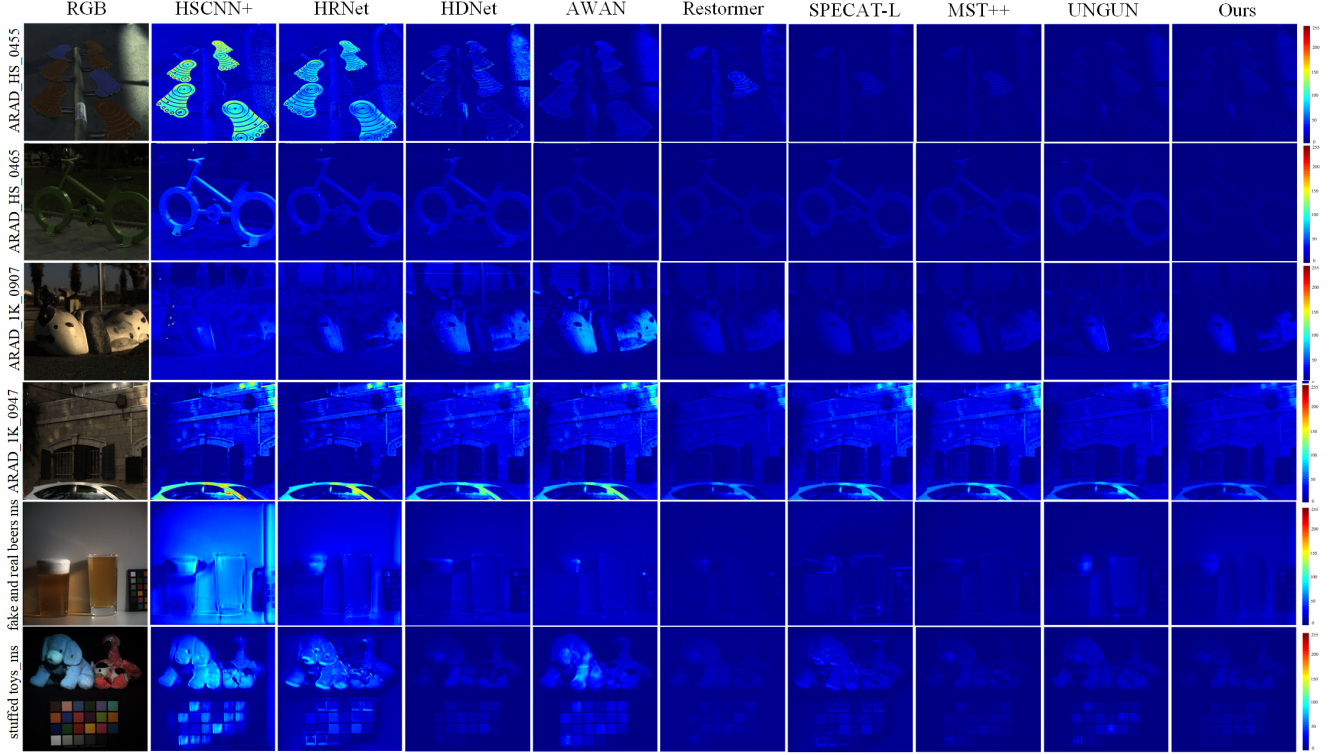


Figure 3. **Visual Comparison Results.** Line 1-2: the RMSE error map of 20-th band on three distinct validation images in NTIRE 2020 Clean. Line 3-4: the RMSE error map of 21-st band on three distinct validation images in NTIRE 2022. Line 5-6: the RMSE error map of 5-th band on two distinct validation images in CAVE.

where the sam represents the spectral angle mapper (SAM) to quantify spectral similarity between query code and \mathbf{f}^+ or \mathbf{f}^- . Additionally, we also align the geometric distribution in the "Reconstruction" phase with relative geometric position.

$$\mathcal{L}_{geo}(\mathcal{G}_{R \rightarrow H}, \mathcal{G}_{H \rightarrow R}) = \mathbb{E}_{h \sim H, \tau \sim R} \left[-\log \frac{\text{sim}(\mathbf{f}, \mathbf{f}^+)}{\text{sim}(\mathbf{f}, \mathbf{f}^+) + \sum_{i=1}^N \text{sim}(\mathbf{f}, \mathbf{f}_i^-)} \right] \quad (18)$$

in which $\text{sim}(u^T, v) = \exp(\frac{u^T v}{\|u\| \|v\| \tau})$ represent the cosine similarity function and τ is the temperature parameter.

3.4. More Details of Framework

Given the absence of paired RGB-HSIs, constructing pixel-wise constraints directly becomes infeasible. As a result, NukesFormers are compelled to build more implicit or indirect constraints to optimize the $\mathcal{G}_{R \rightarrow H}$ and $\mathcal{G}_{H \rightarrow R}$.

Adversarial Loss. Obviously, the absence of direct constraints on the intermediate outputs, $\hat{\mathbf{X}}_f$ and $\hat{\mathbf{Y}}_f$, causes the reconstruction results of NukesFormers to resemble features of the latent space more than HSIs. Recognizing this, we introduce the adversarial loss. By feeding both the reconstructed and real dual-domain images from the dataset

into \mathcal{L}_{adv} , we aim to ensure that the final results are HSIs embodying the right spatial and spectral distribution, not merely feature maps.

$$\mathcal{L}_{adv}^{hsi} = \mathbb{E}_{r \sim H} \log D_H(\mathbf{X}) + \mathbb{E}_{f \sim H} [\log(1 - D_H(\hat{\mathbf{X}}_f))] \quad (19)$$

Similar to other cycle-based methods [7, 41], \mathcal{L}_{adv}^{hsi} makes the reconstructed-HSI similar to real distribution in HSI domain. And the dual-domain adversarial loss is calculated by $\mathcal{L}_{adv} = \mathcal{L}_{adv}^{hsi} + \mathcal{L}_{adv}^{rgb}$.

Non-degraded Loss. Furthermore, inspired by the non-degradable properties of the spectrum, we introduced non-degraded loss to independently constrain $\mathcal{G}_{R \rightarrow H}$ and $\mathcal{G}_{H \rightarrow R}$. Specifically, when an RGB image undergoes the process represented by $\mathcal{G}_{H \rightarrow R}$, which denotes spectral degradation, its spectral features remain aligned, and the converse is also true. Consequently, \mathcal{L}_{nde} is used to separately ensure their functional reliability.

$$\mathcal{L}_{nde} = \mathbb{E}_{r \sim R} [\|\hat{\mathcal{G}}_{R \rightarrow H}(\mathbf{X}) - \mathbf{X}\|_2^2] + \mathbb{E}_{h \sim H} [\|\hat{\mathcal{G}}_{H \rightarrow R}(\hat{\mathbf{Y}}) - \hat{\mathbf{Y}}\|_2^2] \quad (20)$$

Notes that $\hat{\mathcal{G}}_{R \rightarrow H}$ and $\hat{\mathcal{G}}_{H \rightarrow R}$ represent the $\mathcal{G}_{R \rightarrow H}$ and $\mathcal{G}_{H \rightarrow R}$ removed the first up and downsampling operator.

Table 1. The experimental results of NTIRE 2020 Clean, NTIRE2022, and CAVE datasets in UnHIG. The best and second best results are **highlighted** and underlined as below. The existing unpaired framework, UnGUN, is divided with the line. * represents the SRF is unavailable in this dataset.

Method	NTIRE 2020 Clean				NTIRE 2022				CAVE		
	RMSE	MRAE	PSNR	SSIM	RMSE	MRAE	PSNR	SSIM	RMSE	PSNR	SSIM
HSCNN+	0.0976	0.3312	19.53	0.7002	0.1124	1.2473	20.68	0.4107	0.0739	22.86	0.7123
HRNet	0.0597	0.2346	24.93	0.8329	0.0991	0.9019	22.10	0.5282	0.0690	24.09	0.7392
HDNet	0.0467	0.1763	27.57	0.8862	0.0646	0.7537	25.22	0.8049	0.0402	28.14	0.8869
AWAN	0.0475	0.1897	26.98	0.8711	0.0778	0.7916	23.69	0.7143	0.0528	26.02	0.7951
Restormer	0.0389	<u>0.1523</u>	29.20	0.9082	<u>0.0573</u>	0.7285	<u>26.69</u>	<u>0.8350</u>	<u>0.0399</u>	<u>28.75</u>	0.9098
SPECAT-L	0.0408	0.1617	28.89	0.9102	0.0637	0.7528	26.22	0.8288	0.0412	28.30	<u>0.9111</u>
MST++	0.0384	0.1542	<u>29.24</u>	0.9113	0.0609	<u>0.7002</u>	26.46	0.8264	0.0405	28.28	0.9107
UnGUN	<u>0.0362</u>	0.1675	28.63	<u>0.9248</u>	0.0793*	0.7832*	25.04*	0.7942*	0.0477	27.93	0.8832
Ours	0.0312	0.1476	30.55	0.9420	0.0528	0.4829	27.17	0.8526	0.0386	29.57	0.9275

To sum up, the \mathcal{L}_{total} is defined as below:

$$\begin{aligned} \mathcal{L}_{total} = & \lambda_1 * \mathcal{L}_{cyc} + \lambda_2 * \mathcal{L}_{nde} \\ & + \lambda_3 * \mathcal{L}_{adv} + \lambda_4 * \mathcal{L}_{spec} + \lambda_5 * \mathcal{L}_{geo} \end{aligned} \quad (21)$$

in which the λ_i represented as hyper-parameters. The specific setting in our experiment is provided in next session.

4. Experiments

4.1. Experimental Setting

In comparison experiments, we select three benchmark dataset, consisting of NTIRE 2020 Clean Track [1], NTIRE 2022 [2] and CAVE [36].

To demonstrate the efficiency and adaptability of our proposed framework, we integrate HSCNN+ [32], HRNet [40], HDNet [16], AWAN [19], Restormer[39], and MST++ [5] as feature extraction units using existing state-of-the-art methods. In addition, another unpaired method UnGUN [29].

During the experiment, the optimal learning rate was adopted for all the experiments. Based on this foundation, **Ours** adopts $n = \{1, 2, 4, 2, 1\}$. Furthermore, to balance the learning process between the generator and discriminator, the default loss weights were set as $\lambda_1 = \lambda_3 = 1.0$, $\lambda_2 = 0.5$ and $\lambda_4 = \lambda_5 = 0.25$.

Regarding the experimental environment, our work was conducted on the Pytorch platform utilizing the NVIDIA 4090 GPU. The Adam optimizer and cosine learning rate, consisting of $\beta_1 = 0.9$, $\beta_2 = 0.999$ and initial learning rate $lr_{init} = 0.0002$, were employed as the primary optimization

mechanisms during the experiment. Additionally, our methods were trained with $batch_size = 1$ and $epoch = 200$.

4.2. Performance Evaluation

In this section, we segment the experimentation into two distinct parts: firstly, to validate the reliability and robustness of the NukesFormers against existing models, and secondly, to assess the UnHIG performance with ablation experiments. The results offer a holistic testament to the efficacy of the NukesFormers under the UnHIG paradigm, underscoring its superior performance in practical applications.

4.2.1. Comparative Experiments

Notably, CNN-based approaches often require a vast number of parameters, which implies they need meticulous hyper-parameter tuning when training in unpaired task. Comparatively, the Transformer-based method, as indicated in Fig.2, presents a darker overall error map, indicating its superior reconstruction effect.

In the realm of hyperspectral tasks, KANs are capable of more naturally learning intricate high-dimensional mapping through the utilization of B-Spline. To further augment the fitting capacity of KANs for the reconstruction of diverse hyperspectral objects, a non-uniform control point matrix is incorporated. On the NTIRE 2020 Clean Track, as presented in Table 1 and Table 2, our proposed method outperforms sub-optimal approaches across all evaluation metrics. Specifically, it yields a reduction of 0.0050 in the RMSE, a reduction of 0.0047 in the MRAE, an improvement of 1.31 in the PSNR, and an improvement of 0.0172 in the SSIM.

Table 2. The comparison experimental results of Three datasets about four metrics and parameters. The best and second best results are **highlighted** and underline.

*	Params(M)		NTIRE 2020	NTIRE 2022	CAVE
	Train	Infer	SAM	SAM	SAM
HSCNN+	6.09	2.71	8.35	11.33	19.35
HRNet	44.41	41.16	6.01	10.70	16.58
HDNet	6.15	2.67	5.89	9.93	13.55
AWAN	8.40	4.04	5.36	10.06	15.72
Restormer	10.00	6.79	4.40	9.78	11.60
SPECAT-L	4.59	1.46	4.11	10.09	12.98
MST++	6.18	1.62	4.46	9.21	11.40
UnGUN	0.15	0.15	4.17	11.05	11.52
Ours	<u>4.54</u>	<u>1.35</u>	3.97	8.28	9.65

Additionally, in the comparative experiments, the number of parameters of our method ranks second.

Furthermore, when contrasted with other UnHIG frameworks, our method exhibits substantial enhancements on the NTIRE 2022 dataset, which is devoid of additional priors. This superiority can be attributed to our approach’s consideration of both spectral and geometric properties to guide the alignment process.

4.2.2. Ablation Analysis

Ablation analysis is conducted by the setting in Table 2. In order to demonstrate the value of Nukes compared with the traditional KANs, we design the ablation experiment about the Non-Uniform KANs in Table 4.

Table 3. The ablation experimental results of NTIRE 2022 dataset. The best and second best results are **highlighted** and underlined.

Ablation	Params train(M)	NTIRE 2022			
		RMSE	MRAE	PSNR	SSIM
Base	6.01	0.0742	0.8001	25.80	0.7653
Nukes	5.87	0.0723	0.7996	25.99	0.7815
G-MSA	4.42	<u>0.0574</u>	<u>0.5139</u>	<u>27.09</u>	0.8334
DCPM-G	4.54	0.0634	0.5816	26.93	<u>0.8357</u>
DCPM-S	<u>4.53</u>	0.0623	0.6027	25.83	0.8174
Ours	4.54	0.0528	0.4829	27.17	0.8526

As demonstrated in Table 3, **Ours** achieved the best reconstruction performance. To gain a more in-depth understanding of the role of each module, the two branches of DCPM are removed in **DCPM-Geometry** and **DCPM-Spectrum** to analyse their influence for reconstruction. When examining the results, we observe the following changes upon the removal of specific components from the model: With the removal of DCPM-Geometry (DCPM-G), both RMSE and MRAE increase by 0.0106 and 0.0987 respectively. Similarly, upon the removal of DCPM-Spectrum (DCPM-S), we again notice an increase of 0.0095 in RMSE and 0.1198 in MRAE.

In terms of parameter during training, it might seem at first glance that Ours possesses more parameters than the current leading data-driven HIG methods [5, 19, 39]. However, during the testing phase, NukesFormers relies solely on the $\mathcal{G}_{R \rightarrow H}$. Importantly, \mathcal{L}_{adv} is also not used during testing, which significantly reduces its parameter count to 1.35M.

In contrast to existing KANs, Nukes meticulously takes into account the characteristic bands of hyperspectral targets through the embedding of dynamically adjustable control-point matrices. The control points introduced by the NCPG effectively steer the direction of attention in diverse scenarios. Moreover, this empowers the high-dimensional mapping approximated by Nukes to extract more distinctive and valuable features across different scenes and channels, while incurring only a slight increase in the number of parameters.

Table 4. The ablation experimental results about the Nukes and KANs. The best and second best results are **highlighted** and underlined.

Model	Params train(M)	NTIRE 2022		CAVE	
		MRAE	PSNR	RMSE	PSNR
KANs	2.66	0.7882	24.07	0.0544	26.45
Nukes	<u>2.91</u>	0.7523	25.61	0.0512	27.03
Ours-KANs	4.27	<u>0.6452</u>	<u>26.65</u>	<u>0.0414</u>	<u>27.85</u>
Ours-Nukes	4.54	0.4829	27.17	0.0386	29.57

To further validate the enhancement of Non-Uniform’s capacity for extracting hyperspectral features, particularly in the null space, we carried out two ablation experiments employing traditional KANs and Nukes. Specifically, we initially devised a straightforward Encoder-Decoder architecture that incorporates solely KANs or Nukes along with convolutional layers for upsampling and downsampling operations. This architecture effectively verified the fitting capability of KANs in high-dimensional feature mapping and the attention regulation ability of Non - Uniform across different feature channels. Subsequently, we substituted Nukes with traditional KANs. The experimental results indicated an increase of 0.1623 in the MRAE and a decrease of 0.52 in the PSNR in NTIRE 2022. This evidence demonstrates that Nukes facilitates the model in better recovering null-space details in HIG tasks.

5. Conclusion

In this work, we introduce NukesFormers, a novel framework for UnHIG. The proposed method leverages the RND methodology to systematically partition the complex spectral distribution of objects into range space

and null space. By incorporating non-uniform KANs, the framework effectively extracts and compensates for the spectral attributions within the null space. Furthermore, our model seamlessly integrates the HSI and RGB (or MSI) domains through cross-domain contrastive learning, facilitating enhanced spectral representation and domain alignment. Comparative experiments highlight the superior performance of NukesFormers, underscoring its robustness, reliability, and consistency across diverse scenes.

References

- [1] Boaz Arad, Radu Timofte, Ohad Ben-Shahar, Yi-Tun Lin, and Graham D Finlayson. Ntire 2020 challenge on spectral reconstruction from an rgb image. In *Proceedings of the IEEE/CVF Conference on Computer Vision and Pattern Recognition Workshops*, pages 446–447, 2020. 7
- [2] Boaz Arad, Radu Timofte, Rony Yahel, Nimrod Morag, Amir Bernat, Yuanhao Cai, Jing Lin, Zudi Lin, Haoqian Wang, Yulun Zhang, et al. Ntire 2022 spectral recovery challenge and data set. In *Proceedings of the IEEE/CVF Conference on Computer Vision and Pattern Recognition*, pages 863–881, 2022. 7
- [3] Roman Bresson, Giannis Nikolentzos, George Panagopoulos, Michail Chatzianastasis, Jun Pang, and Michalis Vazirgiannis. Kagnns: Kolmogorov-arnold networks meet graph learning. *arXiv preprint arXiv:2406.18380*, 2024. 2
- [4] Yuanhao Cai, Jing Lin, Xiaowan Hu, Haoqian Wang, Xin Yuan, Yulun Zhang, Radu Timofte, and Luc Van Gool. Coarse-to-fine sparse transformer for hyperspectral image reconstruction. In *European Conference on Computer Vision*, pages 686–704. Springer, 2022. 1
- [5] Yuanhao Cai, Jing Lin, Zudi Lin, Haoqian Wang, Yulun Zhang, Hanspeter Pfister, Radu Timofte, and Luc Van Gool. Mst++: Multi-stage spectral-wise transformer for efficient spectral reconstruction. In *Proceedings of the IEEE/CVF Conference on Computer Vision and Pattern Recognition*, pages 745–755, 2022. 1, 2, 7, 8
- [6] Ting Chen, Simon Kornblith, Mohammad Norouzi, and Geoffrey Hinton. A simple framework for contrastive learning of visual representations. In *International conference on machine learning*, pages 1597–1607. PMLR, 2020. 5
- [7] Xiang Chen, Jinshan Pan, Kui Jiang, Yufeng Li, Yufeng Huang, Caihua Kong, Longgang Dai, and Zhentao Fan. Unpaired deep image deraining using dual contrastive learning. In *Proceedings of the IEEE/CVF Conference on Computer Vision and Pattern Recognition*, pages 2017–2026, 2022. 2, 3, 5, 6
- [8] Yinpeng Chen, Xiyang Dai, Mengchen Liu, Dongdong Chen, Lu Yuan, and Zicheng Liu. Dynamic convolution: Attention over convolution kernels. In *Proceedings of the IEEE/CVF conference on computer vision and pattern recognition*, pages 11030–11039, 2020. 4
- [9] Xinhua Cheng, Nan Zhang, Jiwen Yu, Yinhuai Wang, Ge Li, and Jian Zhang. Null-space diffusion sampling for zero-shot point cloud completion. In *IJCAI*, pages 618–626, 2023. 2
- [10] Lu Chi, Borui Jiang, and Yadong Mu. Fast fourier convolution. *Advances in Neural Information Processing Systems*, 33:4479–4488, 2020. 4
- [11] Shangqi Deng, Liang-Jian Deng, Xiao Wu, Ran Ran, and Rui Wen. Bidirectional dilation transformer for multispectral and hyperspectral image fusion. *Proceedings of the Thirty-Second International Joint Conference on Artificial Intelligence*, pages 3633–3641, 2023. 1
- [12] Renwei Dian, Tianci Shan, Wei He, and Haibo Liu. Spectral super-resolution via model-guided cross-fusion network. *IEEE Transactions on Neural Networks and Learning Systems*, 2023. 1
- [13] Deniz Engin, Anil Genç, and Hazim Kemal Ekenel. Cycle-dehaze: Enhanced cyclegan for single image dehazing. In *Proceedings of the IEEE conference on computer vision and pattern recognition workshops*, pages 825–833, 2018. 2
- [14] Biebele Joslyn Fubara, Mohamed Sedky, and David Dyke. Rgb to spectral reconstruction via learned basis functions and weights. In *Proceedings of the IEEE/CVF Conference on Computer Vision and Pattern Recognition Workshops*, pages 480–481, 2020. 2
- [15] Danfeng Hong, Jing Yao, Chenyu Li, Deyu Meng, Naoto Yokoya, and Jocelyn Chanussot. Decoupled-and-coupled networks: Self-supervised hyperspectral image super-resolution with subpixel fusion. *IEEE Transactions on Geoscience and Remote Sensing*, 2023. 2
- [16] Xiaowan Hu, Yuanhao Cai, Jing Lin, Haoqian Wang, Xin Yuan, Yulun Zhang, Radu Timofte, and Luc Van Gool. Hdnnet: High-resolution dual-domain learning for spectral compressive imaging. In *Proceedings of the IEEE/CVF Conference on Computer Vision and Pattern Recognition*, pages 17542–17551, 2022. 1, 2, 7
- [17] Zhipeng Huang, Zhizheng Zhang, Cuiling Lan, Zheng-Jun Zha, Yan Lu, and Baining Guo. Adaptive frequency filters as efficient global token mixers. In *Proceedings of the IEEE/CVF International Conference on Computer Vision*, pages 6049–6059, 2023. 4
- [18] Xu Jia, Bert De Brabandere, Tinne Tuytelaars, and Luc V Gool. Dynamic filter networks. *Advances in neural information processing systems*, 29, 2016. 4
- [19] Jiaojiao Li, Chaoxiong Wu, Rui Song, Yunsong Li, and Fei Liu. Adaptive weighted attention network with camera spectral sensitivity prior for spectral reconstruction from rgb images. In *Proceedings of the IEEE/CVF Conference on Computer Vision and Pattern Recognition Workshops*, pages 462–463, 2020. 2, 7, 8
- [20] Jiaojiao Li, Yihong Leng, Rui Song, Wei Liu, Yunsong Li, and Qian Du. Mformer: Taming masked transformer for unsupervised spectral reconstruction. *IEEE Transactions on Geoscience and Remote Sensing*, 2023. 2
- [21] Miaoyu Li, Ying Fu, Ji Liu, and Yulun Zhang. Pixel adaptive deep unfolding transformer for hyperspectral image reconstruction. In *Proceedings of the IEEE/CVF International Conference on Computer Vision*, pages 12959–12968, 2023. 4
- [22] Zongyi Li, Nikola Kovachki, Kamyar Azizzadenesheli, Burigede Liu, Kaushik Bhattacharya, Andrew Stuart, and

- Anima Anandkumar. Fourier neural operator for parametric partial differential equations. *arXiv preprint arXiv:2010.08895*, 2020. 4
- [23] Yang Liu, Ziyu Yue, Jinshan Pan, and Zhixun Su. Unpaired learning for deep image deraining with rain direction regularizer. In *Proceedings of the IEEE/CVF International Conference on Computer Vision*, pages 4753–4761, 2021. 2
- [24] Ziming Liu, Yixuan Wang, Sachin Vaidya, Fabian Ruehle, James Halverson, Marin Soljačić, Thomas Y Hou, and Max Tegmark. Kan: Kolmogorov-arnold networks. *arXiv preprint arXiv:2404.19756*, 2024. 2
- [25] Zahra Mahdih, Britten Postma, Lou A Herritt, Raymond F Hamilton Jr, Jack R Harkema, and Andrij Holian. Hyperspectral microscopy of subcutaneously released silver nanoparticles reveals sex differences in drug distribution. *Micron*, 153:103193, 2022. 1
- [26] Hyeonuk Nam, Seong-Hu Kim, Byeong-Yun Ko, and Yong-Hwa Park. Frequency dynamic convolution: Frequency-adaptive pattern recognition for sound event detection. *arXiv preprint arXiv:2203.15296*, 2022. 4
- [27] Taesung Park, Alexei A Efros, Richard Zhang, and Jun-Yan Zhu. Contrastive learning for unpaired image-to-image translation. In *Computer Vision—ECCV 2020: 16th European Conference, Glasgow, UK, August 23–28, 2020, Proceedings, Part IX 16*, pages 319–345. Springer, 2020. 3, 5
- [28] Qiaoying Qu, Bin Pan, Xia Xu, Tao Li, and Zhenwei Shi. Unmixing guided unsupervised network for rgb spectral super-resolution. *IEEE Transactions on Image Processing*, 32:4856–4867, 2023. 2
- [29] Qiaoying Qu, Bin Pan, Xia Xu, Tao Li, and Zhenwei Shi. Unmixing guided unsupervised network for rgb spectral super-resolution. *IEEE Transactions on Image Processing*, 2023. 2, 7
- [30] Resales, Achan, and Frey. Unsupervised image translation. In *Proceedings Ninth IEEE International Conference on Computer Vision*, pages 472–478. IEEE, 2003. 2
- [31] Rebecca Del’Papa Moreira Scafutto, Carlos Roberto de Souza Filho, and Wilson José de Oliveira. Hyperspectral remote sensing detection of petroleum hydrocarbons in mixtures with mineral substrates: Implications for onshore exploration and monitoring. *ISPRS Journal of Photogrammetry and Remote Sensing*, 128:146–157, 2017. 1
- [32] Zhan Shi, Chang Chen, Zhiwei Xiong, Dong Liu, and Feng Wu. Hscnn+: Advanced cnn-based hyperspectral recovery from rgb images. In *Proceedings of the IEEE Conference on Computer Vision and Pattern Recognition Workshops*, pages 939–947, 2018. 7
- [33] Junyu Wang, Shijie Wang, Ruijie Zhang, Zengqiang Zheng, Wenyu Liu, and Xinggong Wang. A range-null space decomposition approach for fast and flexible spectral compressive imaging. *arXiv preprint arXiv:2305.09746*, 2023. 4
- [34] Jie Xie, Leyuan Fang, Cheng Wu, Feng Xie, and Jocelyn Chanussot. Blind spectral super-resolution by estimating spectral degradation between unpaired images. *IEEE Transactions on Geoscience and Remote Sensing*, 2024. 2
- [35] Zhiyang Yao, Shuyang Liu, Xiaoyun Yuan, and Lu Fang. Specat: Spatial-spectral cumulative-attention transformer for high-resolution hyperspectral image reconstruction. In *Proceedings of the IEEE/CVF Conference on Computer Vision and Pattern Recognition*, pages 25368–25377, 2024. 1
- [36] Fumihito Yasuma, Tomoo Mitsunaga, Daisuke Iso, and Shree K Nayar. Generalized assorted pixel camera: post-capture control of resolution, dynamic range, and spectrum. *IEEE transactions on image processing*, 19(9):2241–2253, 2010. 7
- [37] Weihao Yu, Mi Luo, Pan Zhou, Chenyang Si, Yichen Zhou, Xinchao Wang, Jiashi Feng, and Shuicheng Yan. Metaformer is actually what you need for vision. In *Proceedings of the IEEE/CVF conference on computer vision and pattern recognition*, pages 10819–10829, 2022. 3
- [38] Zhiyang Yu, Yu Zhang, Dongqing Zou, Xijun Chen, Jimmy S Ren, and Shunqing Ren. Range-nullspace video frame interpolation with focalized motion estimation. In *Proceedings of the IEEE/CVF Conference on Computer Vision and Pattern Recognition*, pages 22159–22168, 2023. 2
- [39] Syed Waqas Zamir, Aditya Arora, Salman Khan, Munawar Hayat, Fahad Shahbaz Khan, and Ming-Hsuan Yang. Restormer: Efficient transformer for high-resolution image restoration. In *Proceedings of the IEEE/CVF Conference on Computer Vision and Pattern Recognition*, pages 5728–5739, 2022. 7, 8
- [40] Yuzhi Zhao, Lai-Man Po, Qiong Yan, Wei Liu, and Tingyu Lin. Hierarchical regression network for spectral reconstruction from rgb images. In *Proceedings of the IEEE/CVF Conference on Computer Vision and Pattern Recognition Workshops*, pages 422–423, 2020. 1, 2, 7
- [41] Hongyuan Zhu, Xi Peng, Joey Tianyi Zhou, Songfan Yang, Vijay Chandrasekh, Liyuan Li, and Joo-Hwee Lim. Single image rain removal with unpaired information: A differentiable programming perspective. In *Proceedings of the AAAI Conference on Artificial Intelligence*, pages 9332–9339, 2019. 6
- [42] Jun-Yan Zhu, Taesung Park, Phillip Isola, and Alexei A Efros. Unpaired image-to-image translation using cycle-consistent adversarial networks. In *Proceedings of the IEEE international conference on computer vision*, pages 2223–2232, 2017. 2
- [43] Zhiyu Zhu, Hui Liu, Junhui Hou, Huanqiang Zeng, and Qingfu Zhang. Semantic-embedded unsupervised spectral reconstruction from single rgb images in the wild. In *Proceedings of the IEEE/CVF International Conference on Computer Vision*, pages 2279–2288, 2021. 2, 3